9-2019

Centrifugally Spun α-Fe2O3/TiO2/Carbon Composite Fibers as Anode Materials for Lithium-Ion Batteries

Luis Zuniga
The University of Texas Rio Grande Valley

Gabriel Gonzalez
The University of Texas Rio Grande Valley

Roberto Orrostieta Chavez
The University of Texas Rio Grande Valley

Jason C. Myers

Timothy P. Lodge

See next page for additional authors

applied sciences

MDPI

Article

Centrifugally Spun α-Fe_2O_3/TiO_2/Carbon Composite Fibers as Anode Materials for Lithium-Ion Batteries

Luis Zuniga [1], Gabriel Gonzalez [1], Roberto Orrostieta Chavez [1], Jason C. Myers [2], Timothy P. Lodge [3] and Mataz Alcoutlabi [1,*]

1 Department of Mechanical Engineering, University of Texas, Rio Grande Valley, Edinburg, TX 78539, USA
2 CSE Characterization Facility, University of Minnesota, Minneapolis, MN 55455, USA
3 Department of Chemical Engineering and Materials Science and Department of Chemistry, University of Minnesota, Minneapolis, MN 55455, USA
* Correspondence: mataz.alcoutlabi@utrgv.edu; Tel.: +1-956-665-8945

Received: 15 July 2019; Accepted: 23 September 2019; Published: 26 September 2019

Abstract: We report results on the electrochemical performance of flexible and binder-free α-Fe_2O_3/TiO_2/carbon composite fiber anodes for lithium-ion batteries (LIBs). The composite fibers were produced via centrifugal spinning and subsequent thermal processing. The fibers were prepared from a precursor solution containing PVP/iron (III) acetylacetonate/titanium (IV) butoxide/ethanol/acetic acid followed by oxidation at 200 °C in air and then carbonization at 550 °C under flowing argon. The morphology and structure of the composite fibers were characterized using X-ray diffraction (XRD), scanning electron microscopy (SEM), transmission electron microscopy (TEM), energy dispersive X-ray spectroscopy (EDS), X-ray photoelectron spectroscopy (XPS), and thermogravimetric analysis (TGA). These ternary composite fiber anodes showed an improved electrochemical performance compared to the pristine TiO_2/C and α-Fe_2O_3/C composite fiber electrodes. The α-Fe_2O_3/TiO_2/C composite fibers also showed a superior cycling performance with a specific capacity of 340 mAh g^{-1} after 100 cycles at a current density of 100 mA g^{-1}, compared to 61 mAh g^{-1} and 121 mAh g^{-1} for TiO_2/C and α-Fe_2O_3/C composite electrodes, respectively. The improved electrochemical performance and the simple processing of these metal oxide/carbon composite fibers make them promising candidates for the next generation and cost-effective flexible binder-free anodes for LIBs.

Keywords: centrifugal spinning; anode; lithium ion battery; α-Fe_2O_3; TiO_2

1. Introduction

With the commercialization of the lithium-ion battery by Sony in 1991, battery technology experienced an enormous boom; the development of portable cellphones, laptops, cameras, and other electronic devices became more common. Lithium-ion batteries (LIBs) are not limited to portable electronic devices but are also seen as a potential replacement for fossil fuels. They are considered a cleaner energy source for electric vehicles, and viable energy storage for wind turbines and other large-scale applications [1,2]. With the increase of research for the application of LIBs in these areas, improvement in battery chemistry becomes imperative. To this end, 1D and 2D-nanostructures such as nanoparticles, nanofibers, carbon nanotubes, and graphene have been widely proposed as alternative electrode materials for LIBs [3–6] and supercapacitors [7–10]. Several groups have focused on the use of nanotechnology to improve existing lithium-ion battery technology, by taking advantage of the large surface area to volume ratio of nanostructured materials [11–13]. An increase in surface area increases the number of reactive sites available for lithium intercalation, thus improving battery capacity and performance. While nanotechnology can be used in many aspects of LIBs, most research has focused on the anode material [6,14,15]. Graphite has been extensively used as the anode material

in commercial LIBs due to its low intercalation/deintercalation potential, long cycle life, and low cost. However, the low theoretical capacity of the graphite anode (372 mA g^{-1}) requires the development of higher capacity anodes for high performance LIBs [1,16–19]. Furthermore, the low operating voltage of the graphite anode leads to the formation of dendritic lithium on the graphite anode, resulting in serious safety problems and cycling instability [20].

Various metal oxides have been investigated as potential candidates for next-generation LIB anode materials due to their superior lithium storage properties, between 500 and 1000 mAh g^{-1}, and abundance [5,21,22]. In particular, TiO_2 and Fe_2O_3 are very promising anode materials, due to their low cost and acceptable charge/discharge capacities [15,23–26]. TiO_2 stores Li via the insertion reaction mechanism, and it exhibits different crystal structures such as anatase, rutile, brookite, and TiO_2 (B) (bronze) [22,27]. The most desired crystalline structure is anatase, due to its superior lithiation ability [28]. TiO_2-based anodes also exhibit low volume expansion (< 4%) [29] upon repeated charge/discharge cycles, due to the layered crystalline structure and high lithium insertion potential of 1.5–1.7 V vs. Li/Li+, which eliminates the potential for both dendrite formation and gas formation due to electrolyte reactions [5,16,30]. Recently, Schweidler et al. [31] conducted a combined operando X ray diffraction and in situ pressure analysis study on a graphite anode. The results showed that the total volume expansion of the graphite anode was 13.2% when C_6 was fully lithiated to LiC_6. In addition, anatase TiO_2 is considered the most electroactive Li-insertion host for Li and has rapid Li insertion/de-insertion kinetics [15]. However, some drawbacks include low electrical conductivity, due to its semi-conductive properties, poor electron transport, and modest theoretical capacity of 333 mAh g^{-1} [1,22,28]. Integrating TiO_2 with a more conductive metal-oxide with a higher theoretical capacity can improve the capacity and electrochemical performance of the TiO_2 anode. Fe_2O_3 is a transition metal oxide that follows a conversion reaction mechanism during electrode reactions [27,32]. Iron oxide, such as hematite Fe_2O_3, exhibits a high theoretical capacity of 1007 mAh g^{-1} [4,13,33–36] and high energy density and has been widely used as an anode material for LIBs, due to its low cost and non-toxicity [32,37,38]. In contrast to TiO_2, this metal oxide suffers a large volume expansion, which can lead to a rapid capacity decay upon cycling, making it an unstable material [3,37–39]. Therefore, combining the high capacity of Fe_2O_3 with the structural stability of TiO_2 in a binary system could result in a promising Fe_2O_3/TiO_2 composite anode material for LIBs. Several research groups have recently reported results on Fe_2O_3/TiO_2 composite anodes for LIBs [4,13,33,34,36,40]. For example, Wang et al. [36] synthesized a binary system of Fe_2O_3/TiO_2 for use in LIBs. The results reported by Wang et al., showed that the Fe_2O_3/TiO_2 anode delivered a specific capacity of 642 mAh g^{-1} at a current rate of 100 mAh g^{-1}.

Another way to improve LIB performance has been to develop nanostructured and binder-free anodes such as electrospun nanofibers, graphene composites, carbon nanotubes, or nanowires [6,41,42]. As opposed to anodes produced by coating conductive powder materials in the form of a slurry on a copper current collector, binder-free anodes eliminate the need for a non-conductive binder, which in return increases the electronic conductivity [22,43,44]. In fact, powder materials (e.g., graphite) have a long diffusion path for lithium-ions and slow electrode reaction kinetics, and as a result, the performance of LIBs has not reached its full potential. Therefore, the use of flexible and binder-free electrodes, such as composite nanofibers, could overcome the problems associated with current commercial graphite anodes due to the fact that they have a shorter diffusion path relative to the commonly employed powder materials, and faster intercalation kinetics is expected, due to their high specific area [15].

In this work, we seek to fabricate ternary α-Fe_2O_3/TiO_2/C binder-free anodes via the centrifugal fiber-spinning (CF) [22,45–51] method followed by subsequent thermal treatment. The prepared composite fibers were characterized using SEM, TEM, XRD, EDS, and XPS. The electrochemical measurements demonstrate that the α-Fe_2O_3/TiO_2/C composite fibers exhibit good cycling performance and rate capability.

2. Materials and Methods

2.1. Materials

Poly (vinylpyrrolidone) with an average molecular weight (M_w) of 1,300,000, acetic acid (≥99%), ethanol (99.5%) (200 proof), titanium (IV) butoxide (97%), and iron (III) acetylacetonate (97%) were all purchased from Sigma-Aldrich (St. Louis, MO, USA). Lithium foil, lithium hexafluorophosphate ($LiPF_6$) (98%), ethylene carbonate (EC) (99%), and dimethyl carbonate (DMC) (99%) were purchased from MTI Corp. (Richmond, CA, USA).

2.2. Preparation of Metal-oxide/Carbon Fibrous Mats

The metal-oxide/carbon composite fibers were prepared by the centrifugal spinning of precursor solutions. The TiO_2/C, Fe_2O_3/C and Fe_2O_3/TiO_2/C composite-fiber anodes were prepared from precursor solutions as follows: For the preparation of TiO_2/C composite fibers, a PVP solution (15 wt%) in ethanol and acetic acid (10:1 ratio) was prepared by stirring for 4 h. One g of titanium (IV) butoxide was added to the solution and stirred for another 12 h to obtain a homogeneous solution before centrifugal spinning. The Fe_2O_3/C composite fibers were prepared from a PVP solution (15 wt%) in a mixture of ethanol and acetic acid with a 10:1 ratio and then stirred for 4 h. Next, 1.5 g of iron (III) acetylacetonate was added to the solution and then stirred for an additional 12 h. Fe_2O_3/TiO_2/C precursor fibers were prepared from a 15 wt% PVP solution in ethanol and acetic acid (10:1 ratio) and stirred for 4 h. 1 g of titanium (IV) butoxide and 1.5 g of iron (III) acetylacetonate were then added to the PVP solution and then stirred for an additional 12 h. The precursor solutions were prepared at room temperature. The TiO_2/C, Fe_2O_3/C, and Fe_2O_3/TiO_2/C composite-fiber anodes were fabricated by the centrifugal spinning of the corresponding precursor solutions followed by thermal treatment. Figure 1 shows a schematic of the centrifugal spinning process and the collected fibers and the as-prepared composite fibers. The CF method relies on applying centrifugal forces to a polymer solution contained in a spinneret rotating at a high rotational speed of up to 10,000 rpm. The polymer solution is forced to exit the nozzle orifice of the spinneret, and the resulting polymer fibers are deposited on the collector as shown in Figure 1A. A description of the CF spinning method was given in a previous work [22,47,48]. In brief, 2 mL of the prepared solution was injected into the needle-based spinneret equipped with 30-gauge half-inch regular bevel needles (Figure 1). The rotational speed of the spinneret was kept at 7000 rpm during the CF of all the solutions. The produced fibers were then collected using a 4 × 4 in cardboard square covered with a spun-bond polypropylene substrate. Figure 1 shows the fibers formed before and after collection. Once the composite fibrous mat was collected, it was then removed from the substrate and dried at 120 °C in a vacuum oven for 12 h prior to carbonization. For the preparation of the composite-fiber electrode, the centrifugally spun fibers were dried and then stabilized in air at 200 °C for 2 h (with a heating rate of 2 °C/min), followed by carbonization at 550 °C for 5 h in an argon atmosphere to obtain the final metal-oxide/carbon composite fibrous mat.

2.3. Characterization

The morphology of the Fe_2O_3/TiO_2/carbon composite fibers was characterized by scanning electron microscopy (SEM) using a Sigma VP Carl Zeiss instrument, coupled with an energy dispersive spectroscopy (EDS) system (EDAX, Mahwah, NJ, USA) to investigate the elemental composition of the fibers. Transmission electron microscopy (TEM) images and selected area electron diffraction (SAED) images were recorded using a FEI G2 F30 microscope operated at 300 kV. High-angle annular dark field (HAADF) scanning TEM (STEM) and EDS maps were collected with a FEI G2 Titan 60–300 probe corrected microscope equipped with a Super-X EDS system. The Titan was operated at 200 kV with a convergence angle of 24 mrad and HAADF inner collection angle of 58.5 mrad. X-ray photoelectron spectrometry (XPS) was conducted using a Thermoscientific K-α instrument equipped with monochromatized Al Kα radiation (1486.7 eV). For all the XPS tests, a spot size of 400 μm for the X-ray beam was implemented. To confirm the desired crystal structure of the synthesized metal

oxide/carbon composite fibers, X-ray diffraction analysis with a 2θ range of 20 to 60 degrees was carried out at a scan rate of 1 °C min^{-1}. Thermogravimetric analysis (TA instruments Q500) was carried out to obtain the carbon content in the composite fibers.

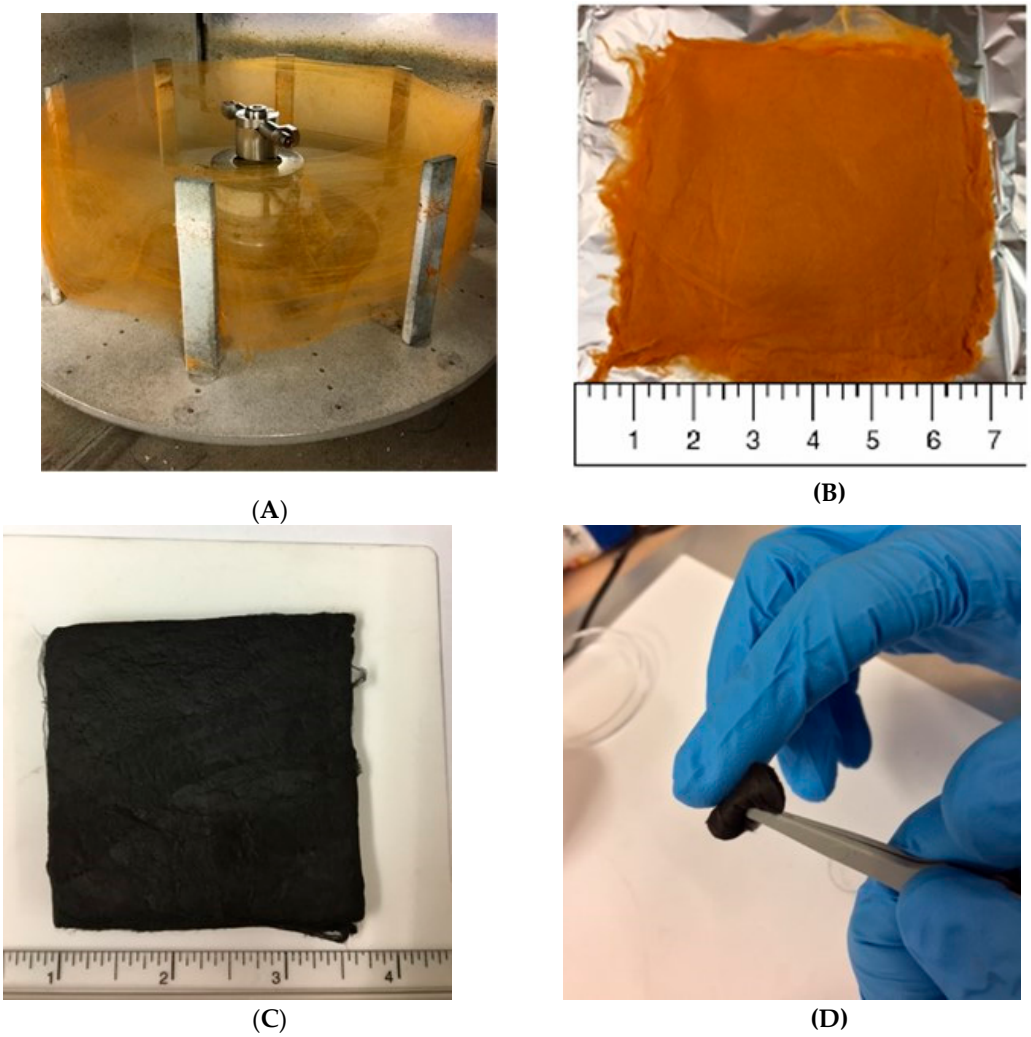

Figure 1. As-spun α-Fe_2O_3/TiO_2/C precursor fibers (**A**); the composite fibrous mat as collected after centrifugal spinning (**B**); the composite fibers after the carbonization process (**C**); free-standing and binder free α-Fe_2O_3/TiO_2/C composite fibers held with a tweezer (**D**). The composite fiber anodes show excellent flexibility.

2.4. Electrochemical Performance Evaluation

The electrochemical performance of the composite fiber anodes was investigated using 2032 coin-type cells. The free-standing fiber anodes had a weight ranging from 3 to 7 mg. Lithium metal chips were used as the counter electrode, while glass microfibers were used as the separator. The electrolyte used consisted of 1 mol/L $LiPF_6$ salt in EC/DMC (1:1 by volume) solvent. The coin cells were then assembled in a high purity argon-filled glove box (Munich, Mbraun, Germany) with O_2 and H_2O concentrations of < 0.5 ppm. The composite-fiber anode is 1 cm in diameter and 100–300 microns in thickness, depending on the weight of the free binder electrode (the mass of the composite fiber anode is usually between 2 mg to 4 mg). Next, 6 to 10 drops of the liquid electrolyte were added to each cell during the cell assembly in the glove box. The electrochemical performance was evaluated by carrying out galvanostatic charge-discharge experiments on using CR2032 coin type cells at a current density of 100 mA g^{-1} between 0.05 and 3.0 V using a LANHE CT2001A battery testing system.

The applied cycling current and specific charge/discharge capacities were calculated based on the mass of the composite-fiber anodes. Cyclic voltammetry was carried out using Biologic BCS-810, and electrochemical impedance experiments were performed using Autolab 128 N with a scan rate of 0.2 mVs^{-1} and at frequencies from 0.1 Hz–1 kHz. Finally, rate performance tests were carried out on coin cells at current densities of 50, 100, 200, 400, and 500, mA g^{-1} using an Arbin battery testing system. The current density was calculated with respect to the mass of the binder free electrode.

3. Results and Discussion

3.1. Morphology

Scanning electron microscopy (SEM) and energy dispersive spectroscopy (EDS) were used to analyze the morphology and elemental composition of the composite fibers. Figures 2–4 show the SEM images with different magnifications of the α-Fe_2O_3/C, TiO_2/C, and α-Fe_2O_3/TiO_2/C composite nanofibers. For the α-Fe_2O_3/C composite fibers, it was appreciated that after calcination, these fibers possessed a rough textured surface while maintaining a solid cross-section. Upon carbonization, the TiO_2/C fibers showed a smooth solid fiber morphology, as seen in the SEM images. The cross section of the Fe_2O_3/TiO_2/C composite fibers demonstrated a degree of porosity within the fibers, in contrast to the Fe_2O_3/C and TiO_2/C composite fibers shown in Figures 2 and 3.

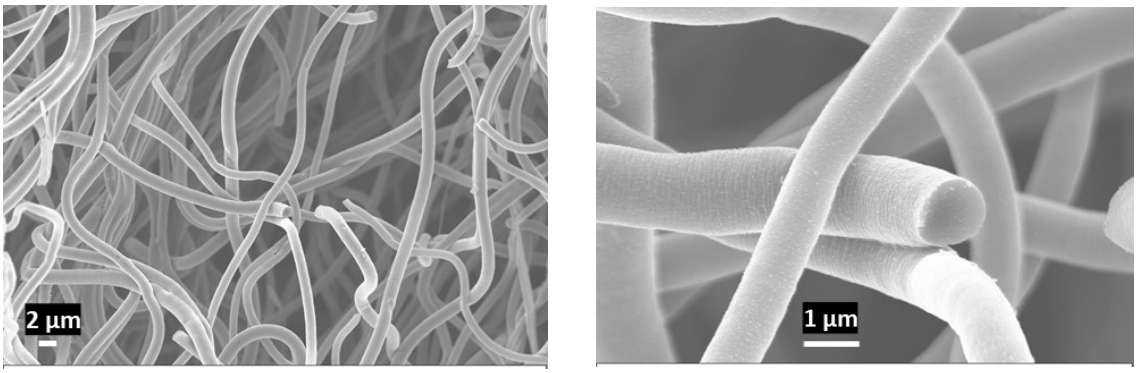

(**A**) (**B**)

Figure 2. SEM images of the α-Fe_2O_3/C composite fibers after heat treatment. Magnification: (**A**) 5000× and (**B**) 30,080×.

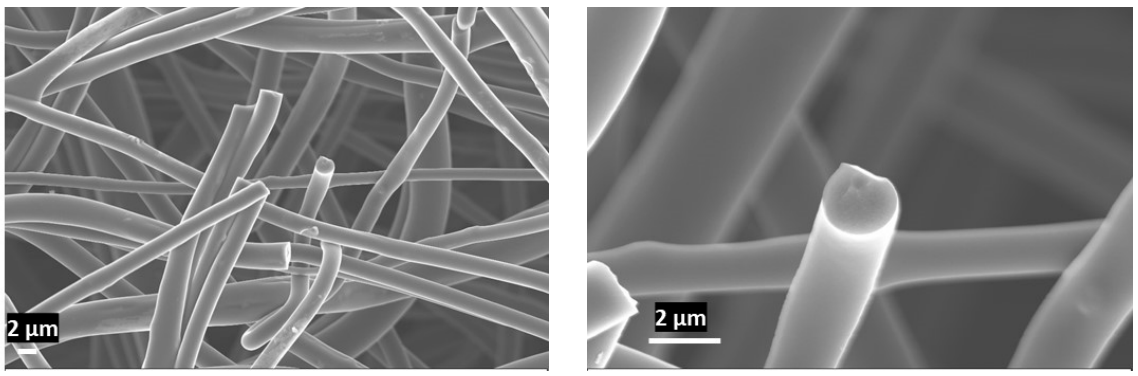

(**A**) (**B**)

Figure 3. SEM images of the TiO_2/C composite fibers after heat treatment. Magnification: (**A**) 5000 and (**B**) 20,000.

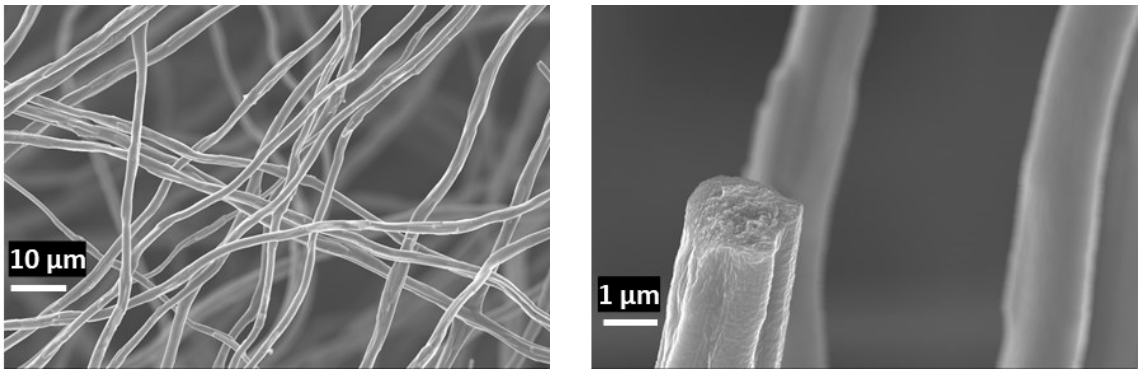

(**A**) (**B**)

Figure 4. SEM images of the ternary α-Fe_2O_3/TiO_2/C composite fibers after heat treatment. Magnification: (**A**) 3000 and (**B**) 30,000.

The crystal structure and morphology of the α-Fe_2O_3/TiO_2/C composite fibers were further analyzed using TEM and HRTEM, as shown in Figure 5A,B. The TEM image of the α-Fe_2O_3/TiO_2/C carbon composite fibers shows the α-Fe_2O_3/TiO_2 nanoparticles being deposited on the surface of carbon fibers. Figure 5B shows a typical high-resolution TEM (HRTEM) image taken from the α-Fe_2O_3/TiO_2 nanoparticles on carbon fibers. The most common spacing in the TEM images is in the 0.34–0.35 nm range, which corresponds to the (101) anatase spacing. Figure 6B also shows crystalline lattice spacings of 0.24 nm and 0.27, which correspond to the 004 and 104 crystalline planes of anatase and Fe_2O_3, respectively. The particles were heavily agglomerated in all images but were estimated to have diameters of 3–5 nm. The 3.25 A fringes on the larger particles do match the (110) spacing for anatase.

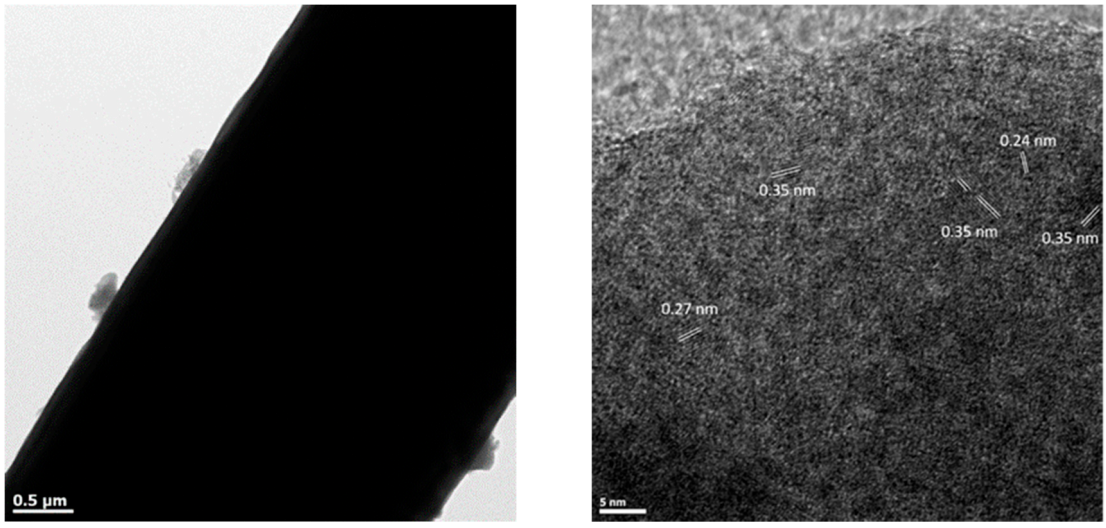

(**A**) (**B**)

Figure 5. TEM images of Fe_2O_3/TiO_2/C composite fibers showing (**A**) aggregates of crystalline material on the surface of the fiber and (**B**) polycrystalline structure of one of these aggregates.

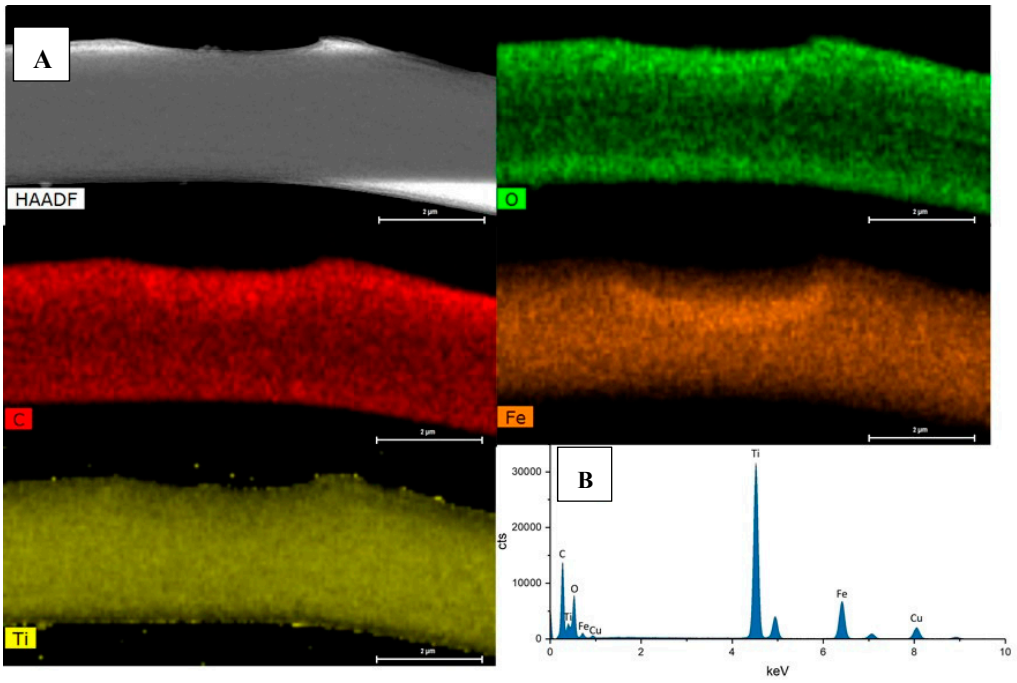

Figure 6. (**A**) HAADF-STEM image for a selected area with corresponding EDS maps for O, C, Fe, and Ti elements. (**B**) EDS spectrum of $Fe_2O_3/TiO_2/C$ composite fibers.

The energy dispersive X-ray spectrometry (EDS) mapping images and HAADF of α-$Fe_2O_3/TiO_2/C$ composite fibers (Figure 6) suggest that the α-Fe_2O_3 and TiO_2 nanoparticles and CFs were well-distributed in the as-prepared materials. The TEM elemental maps of the α-$Fe_2O_3/TiO_2/C$ composite fibers confirm that the primary constituent elements are C, Ti, O, and Fe. The phase mapping of the α-$Fe_2O_3/TiO_2/C$ composite-fiber spectra in Figure 6 suggests that the key elements of Ti, Fe, and C are uniformly distributed throughout the composite fibers. Note that the Cu peak in the EDS spectrum (Figure 6B) arises from the sample support TEM grid. Especially in the case of thick samples (200–400 m), such as the composite fibers in this work, a large portion of the electron intensity is scattered to the sides at high angles.

3.2. *Surface Analysis: XPS*

X ray photoelectron spectroscopy was carried out to further evaluate the surface elemental composition of the α-$Fe_2O_3/TiO_2/C$ fibers. Figure 7 shows the general survey as well as the spectra for C (1s), O (1s), Ti (2p), and Fe (2p). Two sharp peaks with binding energies of 710 and 725 eV are observed, which correspond to $Fe^{3+}2p_{2/3}$ and $Fe^{3+}2p_{1/2}$, respectively. Large and broader satellite peaks at 720 and 735 eV are also observed, which are characteristic of α-Fe_2O_3. For the Ti (2p) spectrum, the peaks at 458 and 464 eV correspond to $Ti^{4+}2p_{3/2}$ and $Ti^{4+}2p_{1/2}$ of TiO_2, respectively. These distinct peaks revealed the presence of the Ti^{4+} valence state in the prepared fibers. The high carbon content and oxygen component of the metal oxides are also confirmed by XPS analysis.

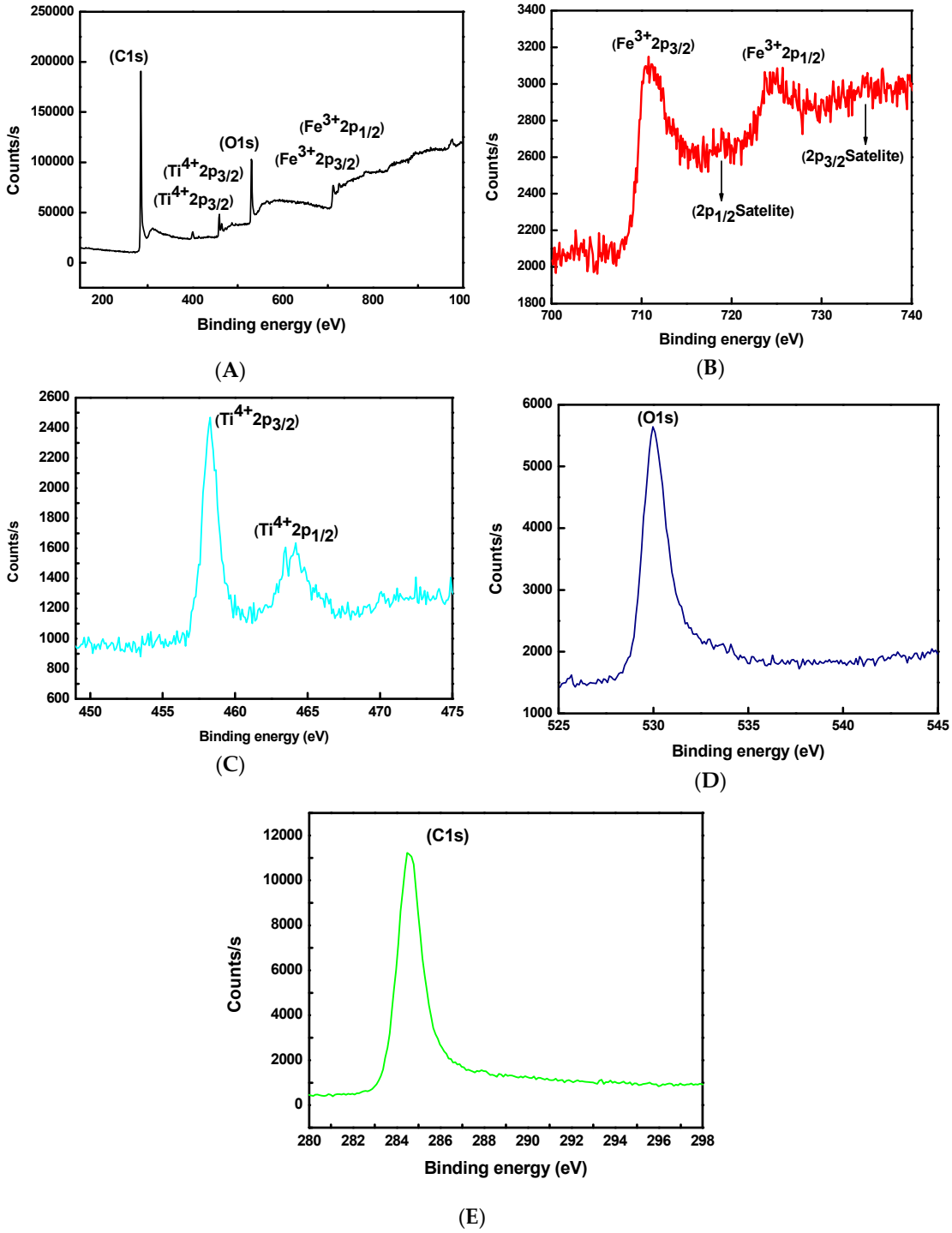

Figure 7. Survey XPS spectrum of the Fe_3O_4/C composite nanofibers (**A**), deconvoluted spectra of nanocomposite structure for Fe 2p (**B**), Ti 2p (**C**), O 1s (**D**), and C 1s (**E**).

3.3. Thermogravimetric and Crystal Structure Analysis

The XRD and TGA results are shown in Figure 8. From the XRD analysis, the pattern for the anatase crystal structure of TiO_2 was confirmed using indexing from (JCPDS 73-1764). The α-Fe_2O_3 crystal structure was also observed and was indexed using (JCPDS 33-0664). The TGA analysis on the α-Fe_2O_3/TiO_2/carbon composite fibers was performed by heating the sample to 750 °C in air at 3 °C/min to completely decompose the carbon component in the sample; the observed weight loss is equal to the carbon content [52].

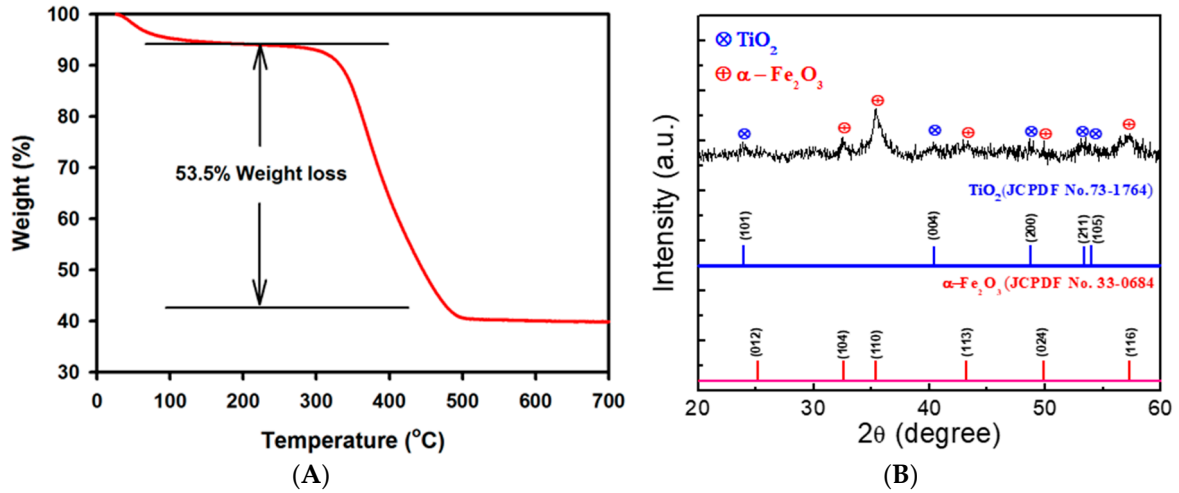

Figure 8. (**A**) Thermogravimetric analysis (TGA) and (**B**) X-ray diffraction patterns of α-Fe_2O_3/TiO_2/carbon composite fibers demonstrating the material crystal structure.

The weight loss that occurred below 100 °C was caused by the loss of adsorbed water in the α-Fe_2O_3/TiO_2/carbon composite fibers. As shown in Figure 8a, the TGA results showed a carbon content of 53.5% while the Fe_2O_3/TiO_2/carbon composite fibers exhibit a weight loss of 59.9%, thereby confirming that the amount of the active material in the composite-fiber anode is about 40.1% of Fe_2O_3 and TiO_2 nanoparticles.

4. Electrochemical Analysis

4.1. Cyclic Voltammetry

To understand the interaction process of Li^+ with the developed ternary composite electrode, cyclic voltammograms (CV) were evaluated for the first four cycles. In this electrochemical test, the oxidation and reduction reactions occurring within the coin cell can be detected and analyzed. Figure 9 shows the CV results for the Fe_2O_3/TiO_2/C composite fibers. For the initial cathodic scan (corresponding to Li^+ insertion), a peak at a potential of 1.8 V is present (R1). This peak can be attributed to the initial insertion of lithium into the α-Fe_2O_3 and TiO_2 components of the electrode, as shown in Equations (1) and (2) [53]:

$$Fe_2O_3 + xLi^+ + xe^- \rightarrow Li_xFe_2O_3 \quad (1)$$

$$TiO_2 + xLi^+ + xe^- \leftrightarrow Li_xTiO_2 \quad (2)$$

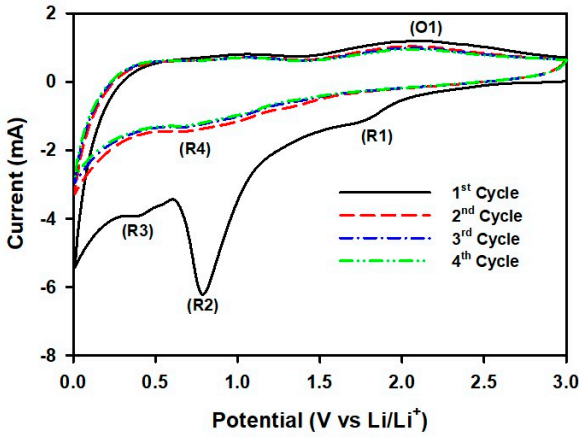

Figure 9. Cycle Voltammetry curves of Fe_2O_3/TiO_2/C composite fibers between 0.01 and 3.0 V at a scan rate of 0.1 mVs^{-1}.

A second reaction can be observed at a potential of 0.8 V (R2), which is attributed to the complete reduction of the Fe_2O_3 to elemental Fe and Li_2O (Equation (3)). The decrease in the peak sharpness confirms the large specific capacity loss during the initial discharge cycle due to the conversion reaction (Equation (3)) [23]:

$$Fe_2O_3 + 6Li^+ + 6e^- \rightarrow 2\,Fe + 3Li_2O. \quad (3)$$

The final irreversible peak observed at the first cycle at a potential of 0.4 V (R3) is attributed to the formation of the solid electrolyte interface (SEI) layer at the electrode/electrolyte interface. In the later cycles, the peaks from the irreversible reactions R1 and R3 are no longer present, where only the reduction and oxidation peaks at 0.8 and 2.1 V are observed (R4, O1). These peaks are associated with the alloying/de-alloying between Li and elemental Fe, as well as the intercalation between lithium ions and TiO_2 and carbon (Equations (2) and (4)):

$$6C + xLi^+ + xe^- \leftrightarrow Li_xC_6 \quad (4)$$

4.2. Electrochemical Performance

In order to evaluate and compare the electrochemical performance of the prepared composite fibers, cycling performance tests were carried out on coin cells for α-Fe_2O_3/C, TiO_2/C, and α-Fe_2O_3/TiO_2/C fibers at a current density of 100 mA g^{-1} over 100 cycles. Figure 10 shows the charge (lithium extraction)/discharge (lithium insertion) curves of the composite fiber anodes. The charge/discharge curves were obtained at a constant current density of 100 mA g^{-1} over a potential window of 0.05–3 V. By comparing the performance between α-Fe_2O_3/C and TiO_2/C, it can be seen that α-Fe_2O_3/C shows a much higher initial capacity of 1735 mAh g^{-1} than TiO_2/C (318 mAh g^{-1}). However, characteristic of α-Fe_2O_3, this anode suffers a tremendous capacity degradation as the capacity quickly drops to 422 mAh g^{-1} at the 2nd cycle and finally to 121 mAh g^{-1} after the 100th cycle. The large capacity fade at the first cycle is attributed to the irreversible reaction characteristic of metal oxides and the formation of the SEI layer, which can be seen in all three composite fiber anodes. In this irreversible process, lithium reacts with oxygen to form lithium oxide, losing useful lithium ions to this by-product and hence leading to severe capacity loss. The later capacity fade is caused by the large volume expansion of the α-Fe_2O_3/C composite-fiber anode upon cycling. The TiO_2/C composite-fiber anode also shows some capacity fading; however, it is not as pronounced as for the α- Fe_2O_3/C composite-fiber anode. This can be attributed to a much more stable structure and minimal volume expansion for the TiO_2. The capacity of 61 mAh g^{-1} for the TiO_2/C anode after the 100th cycles is still lower than that for α-Fe_2O_3/C.

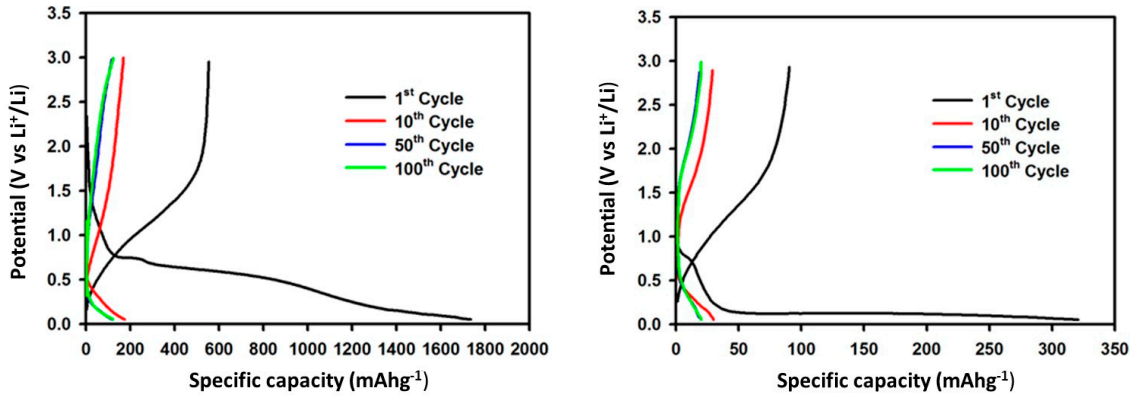

Figure 10. *Cont.*

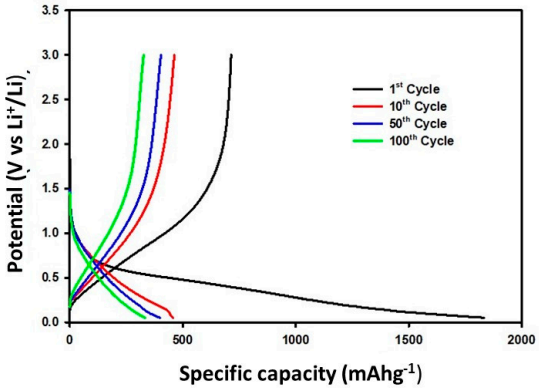

(**C**)

Figure 10. Charge−discharge curves of the composite fibers performed over 100 cycles at a current density of 100 mA g^{-1}. α-Fe_2O_3/C (**A**), TiO_2/C (**B**); α-Fe_2O_3/TiO_2/C (**C**).

The cycling performance of the TiO_2/C, α-Fe_2O_3/C, and α-Fe_2O_3/TiO_2/C composite fiber anodes is shown in Figure 11A,B. The α-Fe_2O_3/TiO_2 composite fiber anode shows a better electrochemical performance than the pristine TiO_2/C anode because the TiO_2 provides structural stability to the composite anode, while maintaining the higher capacity resulting from the addition of the α-Fe_2O_3 to the TiO_2/C fiber precursor. This can be observed by the cycling performance of the ternary α-Fe_2O_3/TiO_2/C composite fibers which showed a high initial capacity of 1832 mAh g^{-1} at the 1st cycle and a capacity of 340 mAh g^{-1} after 100 cycles. The addition of the TiO_2 to the α-Fe_2O_3 fiber precursor helped alleviate the large volume expansion, therefore reducing the capacity fading after subsequent cycles. This proves that combining both metal oxides provide an electrode with improved electrochemical performance and superior cycling stability. While the irreversible reaction at the first cycle provides a low initial coulombic efficiency for all three of the composite fiber anodes, after subsequent cycles, the composite fiber electrodes can maintain a high efficiency of about 97% (Figure 11A). Results reported in the literature showed in some cases that the Fe_2O_3/C electrode delivered lower capacity after 100 cycles than that for the TiO_2 electrode. This poor performance was caused by the high-volume change of the Fe_2O_3 electrode [25]. Several studies showed that the α-Fe_2O_3/TiO_2/C delivered excellent electrochemical performance compared to the α-Fe_2O_3 and TiO_2 electrodes, which was attributed to the synergetic effect between α-Fe_2O_3 and TiO_2 which can improve the diffusion kinetics and structural stability of the electrode [24,25,54,55].

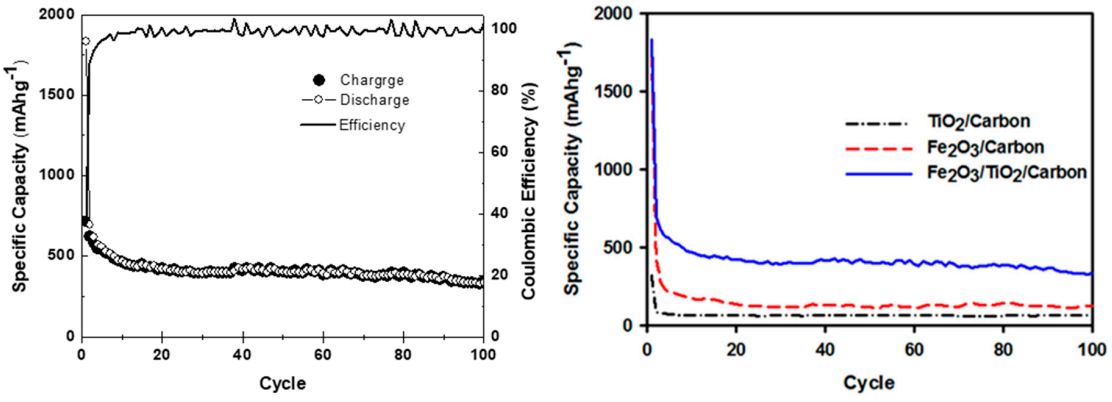

(**A**) (**B**)

Figure 11. Cycling performance of the composite fiber anodes at a current density of 100 mA g^{-1}. (**A**) the cycle performance and coulombic efficiency of the α-Fe_2O_3/TiO_2/C composite fibers, and (**B**) cycling performance of the TiO_2/C, α-Fe_2O_3/C and α-Fe_2O_3/TiO_2/C composite fibers.

The 70% loss in capacity of Fe_2O_3/C and TiO_2/C composite-fiber electrodes observed in Figure 10A,B might be caused by the slow reaction kinetics of these metal oxides and the effect of SEI layer formation at the first cycle. The large volume change of the Fe_2O_3 nanoparticles can also result in loss in capacity of the Fe_2O_3/C composite-fiber electrode after prolonged charge/discharge cycles [54]. Another factor in the loss in the electrode capacity can be the poor conductivity of the TiO_2 and Fe_2O_3 nanoparticles [56]. The aggregation of the Fe_2O_3 and TiO_2 nanoparticles in the carbon-fiber matrix can prevent the access of electrolyte to the active material (in aggregated nanoparticles, the electrolyte has access only to the nanoparticles on the surface and not to the ones covered by other nanoparticles in the aggregated cluster) resulting in capacity loss at an increasing cycle number. Improving the dispersion of active material in the centrifugally spun carbon-fiber matrix and optimizing the structure and morphology of the Fe_2O_3/C and TiO_2/C composite fibers are very important in order to improve the cyclability and electrochemical performance of the composite electrodes. The thickness of the composite-fiber anode can also affect the capacity and electrochemical performance of the composite electrode. Thick fibrous mats will result in the formation of a thick SEI layer at the first cycle thus, resulting in high capacity loss at the first cycle and low capacity retention [57]. These issues will be addressed in a future work.

4.3. Rate Performance

To investigate the rate performance of this composite electrode, CR2032 coin-type cells were cycled at different current densities. The composite fiber electrodes were cycled ten times at current densities of 50, 100, 200, 400, 500 and then again at 50 mA g^{-1}. This was done to evaluate the cycling performance at higher current densities, as well as to observe if the capacity would be recovered from being cycled at high to low current density. Figure 12 shows the rate performance of the ternary α-Fe_2O_3/TiO_2/C electrode. Again, the addition of the stable TiO_2 can improve the electrochemical performance of the ternary electrode by allowing cycling at increased current densities. Maintaining a specific capacity of more than 200 mAh g^{-1} at a current density of 500 mA g^{-1}, this electrode showed excellent cycling stability at elevated current densities. Interestingly, when the α-Fe_2O_3/TiO_2/C composite anode was cycled back at low current density (50 mA g^{-1}), it was able to recover to a specific capacity of 549 mAh g^{-1}, indicating good reversibility. The dispersion of TiO_2 and α-Fe_2O_3 nanoparticles in the carbon matrix helped reduce the severe volume expansion of the iron oxide, resulting in a more stable anode material with exceptional lithium storage abilities.

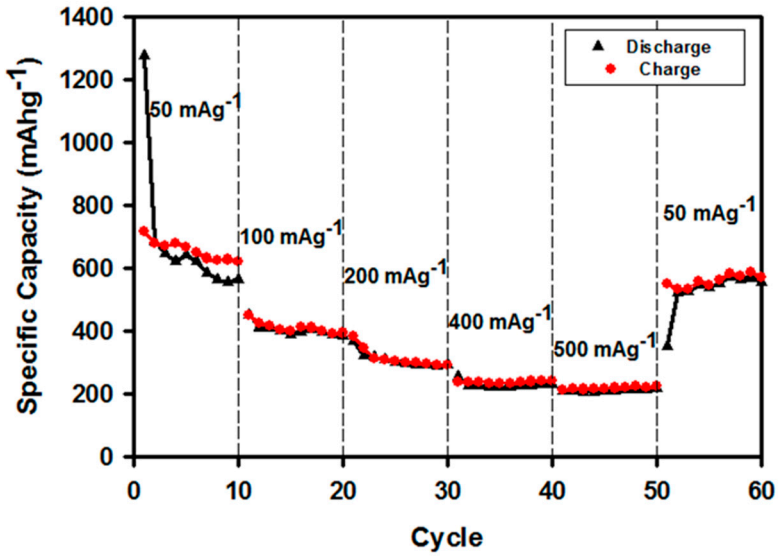

Figure 12. Rate performance for the α-Fe_2O_3/TiO_2/C electrode performed at current densities of 50, 100, 200, 400, and 500 mA g^{-1}. Dashed (charge) and solid (discharge).

4.4. Impedance

To further evaluate the electrochemical performance of the three composite electrodes, electrochemical impedance spectroscopy (EIS) was performed before and after cycling. The Nyquist plots both prior to and post cycling are shown in Figure 13A,B. A typical impedance spectrum (Nyquist plot) of an anode material with the equivalent electrical circuit is shown in Figure 13C,D. The Nyquist plot of the circuit model shows a semicircle in the high and medium frequency regions and a straight line with a constant slope in the low frequency range. The initial intercept value of the semi-circle in the high to medium frequency region represents the impedance (R_s) associated with the resistance of the SEI layer formed on the electrode surface. The semicircle in the middle frequency range can be ascribed to the charge-transfer resistance (R_{ct}) at the electrode/electrolyte interface [57]. The straight line in the low frequency region represents the diffusion properties of Li^+ within the electrode; the slope of which gives the Warburg impedance. Figure 13 shows the characteristic impedance at both low and high frequencies of the Fe_2O_3/C, TiO_2/C and α-Fe_2O_3/TiO_2/C to be an inclined line and semicircle, respectively. The semicircle comprises the combination of the contact resistance between the active material and current collector, the intrinsic resistance of the active materials, and the ionic resistance of the electrolyte, while the inclined line reflects the solid-state diffusion of Li within the electrode. The diameter of the intermediate-frequency semicircle indicates the electrode–electrolyte interfacial resistance R_{CT}.

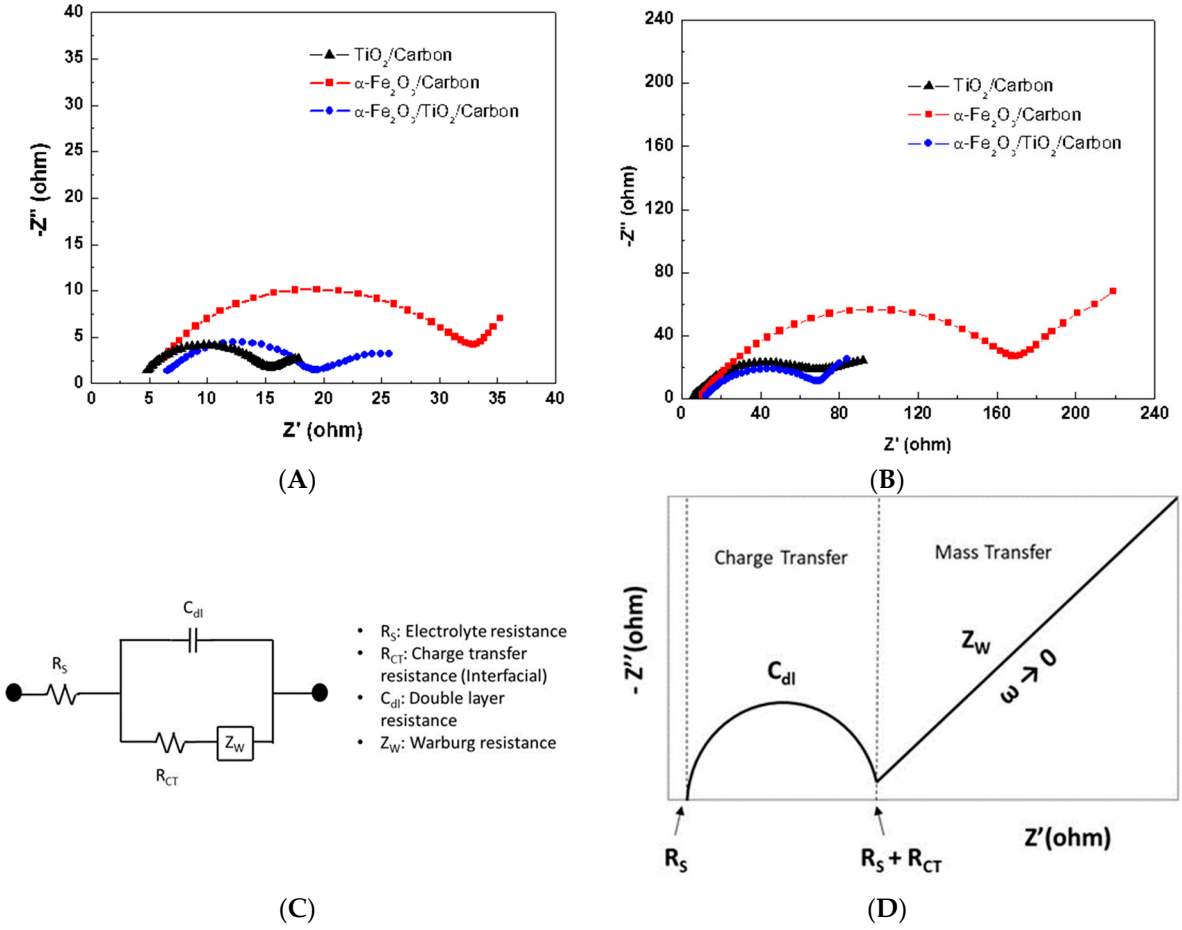

Figure 13. Nyquist plots comparing fresh (**A**) and aged (**B**) electrochemical impedance between the metal oxide/carbon composite electrodes after 100 cycles, (**C**) schematic of equivalent impedance circuit model and (**D**) the corresponding Nyquist plot of the circuit model with all the parameters shown on the plot.

It can be seen in Figure 13 that the electrode (fresh cell) with the highest charge transfer resistance (R_{CT}) was that composed of the α-Fe_2O_3/C fibers, as it showed an impedance of 26. The TiO_2/C and α-Fe_2O_3/TiO_2/C composite electrodes showed much lower impedance values of 11 and 13, respectively. A post-cycling impedance analysis was evaluated (aged cells) to compare the results. Again, the α-Fe_2O_3/C showed greater impedance compared to the other two electrodes where the charge transfer resistance (R_{CT}) of the α-Fe_2O_3/C composite-fiber electrodes was 171. This can be attributed to the poor ion intercalation kinetics of this composite electrode, as well as to the formation of a thick SEI layer. On the contrary, the α-Fe_2O_3/TiO_2/C electrode showed much lower charge transfer resistance (R_{CT} = 56) than that for the TiO_2/C (R_{CT} = 69). and α-Fe_2O_3/C after cycling (R_{CT} = 168). This demonstrates how the stable structure of the TiO_2 nanoparticles improved the ionic transport in the composite-fiber electrode, hence leading to the improved performance. The effect of SEI layer formation on the electrochemical reversibility of graphite anode has been widely studied [58,59]. Our future work will be focused on investigating the effect of surface area of fibers on the first charge capacity of composite-fiber anodes. The effect of the SEI formation at the first discharge cycle on the electrochemical performance of the electrode will be systematically investigated

5. Conclusions

Ternary α-Fe_2O_3/TiO_2/C composite fibers were successfully produced by centrifugal spinning and subsequent thermal processing for use as binder-free anodes for LIBs. The ternary composite fibers were produced from a PVP/iron (III) acetylacetonate/titanium (IV) butoxide/ethanol/acetic acid precursor solution, then heat treated at elevated temperature. These unique composite fiber anodes showed excellent electrochemical performance when compared to TiO_2/C and α-Fe_2O_3/C fibers. The high capacity of α-Fe_2O_3 and the stability of the TiO_2 led to the high performance and excellent cycling stability of the ternary electrode. To the best of our knowledge, these are the first results reported on binder-free α-Fe_2O_3/TiO_2/C composite fibers for use as anodes in LIBs. The mass production of fibers by centrifugal spinning, along with the excellent electrochemical performance and flexibility of these anodes, make these fibers good candidates for next generation electrode materials for high power LIBs.

Author Contributions: L.Z. designed and performed the experiments. G.G. reanalyzed the impedance and cycling performance results. R.O.C. reanalyzed the electrochemical results and reviewed the manuscript. J.C.M. conducted the TEM, EDS, SAED and HAADF scanning experiments and wrote the TEM/EDS characterization section. T.P.L. reviewed the manuscript and provided constructive advising for the project. L.Z., T.P.L. and M.A. wrote the manuscript. M.A. supervised the project.

Funding: This research was funded by NSF PREM award DMR-1523577 and also by UMN MRSEC program under Award Number DMR-1420013.

Acknowledgments: This research is supported by NSF PREM award DMR-1523577: UTRGV-UMN Partnership for Fostering Innovation by Bridging Excellence in Research and Student Success. Part of this work was carried out in the College of Science and Engineering Characterization Facility, University of Minnesota, which has received capital equipment funding from the NSF through the UMN MRSEC program under Award Number DMR-1420013. This research was partially supported by the USDA, the National Institute of Food and Agriculture, and the Integrating Food Science/Engineering and Education Network (IFSEEN) with award number: 2015-38422-24059.

Conflicts of Interest: The authors declare no conflict of interest.

References

1. Li, X.; Chen, Y.; Zhou, L.; Mai, Y.-W.; Huang, H. Exceptional electrochemical performance of porous TiO_2-carbon nanofibers for lithium ion battery anodes. *J. Mater. Chem. A* **2014**, *2*, 3875–3880. [CrossRef]
2. Xin, X.; Zhou, X.; Wu, J.; Yao, X.; Liu, Z. Scalable Synthesis of TiO_2/Graphene Nanostructured Composite with High-Rate Performance for Lithium Ion Batteries. *ACS Nano* **2012**, *6*, 11035–11043. [CrossRef] [PubMed]
3. Aadil, M.; Shaheen, W.; Warsi, M.F.; Shahid, M.; Khan, M.A.; Ali, Z.; Haider, S.; Shakir, I. Superior electrochemical activity of α-Fe_2O_3/rGO nanocomposite for advance energy storage devices. *J. Alloys Compd.* **2016**, *689*, 648–654. [CrossRef]

4. Yu, L.; Wang, Z.; Zhang, L.; Wu, H.B.; Lou, X.W. TiO_2 nanotube arrays grafted with Fe_2O_3 hollow nanorods as integrated electrodes for lithium-ion batteries. *J. Mater. Chem. A* **2013**, *1*, 122–127. [CrossRef]
5. Zhang, X.; Suresh Kumar, P.; Aravindan, V.; Liu, H.H.; Sundaramurthy, J.; Mhaisalkar, S.G.; Duong, H.M.; Ramakrishna, S.; Madhavi, S. Electrospun TiO_2—Graphene Composite Nanofibers as a Highly Durable Insertion Anode for Lithium Ion Batteries. *J. Phys. Chem. C* **2012**, *116*, 14780–14788. [CrossRef]
6. Ji, L.W.; Meduri, P.; Agubra, V.; Xiao, X.C.; Alcoutlabi, M. Graphene-Based Nanocomposites for Energy Storage. *Adv. Energy Mater.* **2016**, *6*, 1502159. [CrossRef]
7. Kasap, S.; Kaya, I.I.; Repp, S.; Erdem, E. Superbat: Battery-like supercapacitor utilized by graphene foam and zinc oxide (ZnO) electrodes induced by structural defects. *Nanoscale Adv.* **2019**, *1*, 2586–2597. [CrossRef]
8. Alas, M.O.; Gungor, A.; Genc, R.; Erdem, E. Feeling the power: Robust supercapacitors from nanostructured conductive polymers fostered with Mn2+ and carbon dots. *Nanoscale* **2019**, *11*, 12804–12816. [CrossRef]
9. Galla, S.; Szewczyk, A.; Smulko, J.; Przygocki, P. Methods of Assessing Degradation of Supercapacitors by Using Various Measurement Techniques. *Appl. Sci.* **2019**, *9*, 2311. [CrossRef]
10. Li, W.; Sun, J.; Wu, Z.; Liu, S. N-Doped Carbon Aerogels Obtained from APMP Fiber Aerogels Saturated with Rhodamine Dye and Their Application as Supercapacitor Electrodes. *Appl. Sci.* **2019**, *9*, 618. [CrossRef]
11. Saravanan, K.; Ananthanarayanan, K.; Balaya, P. Mesoporous TiO_2 with high packing density for superior lithium storage. *Energy Environ. Sci.* **2010**, *3*, 939–948. [CrossRef]
12. Tang, K.; Yu, Y.; Mu, X.; van Aken, P.A.; Maier, J. Multichannel hollow TiO_2 nanofibers fabricated by single-nozzle electrospinning and their application for fast lithium storage. *Electrochem. Commun.* **2013**, *28*, 54–57. [CrossRef]
13. Wang, W.; Bu, F.-X.; Jiang, J.-S. Porous TiO_2 coated α-Fe_2O_3 ginger-like nanostructures with enhanced electrochemical properties. *Mater. Lett.* **2015**, *139*, 89–92. [CrossRef]
14. Meng, J.-K.; Zhao, Q.-Q.; Ye, W.-H.; Zheng, G.-P.; Zheng, X.-C.; Guan, X.-X.; Liu, Y.-S.; Zhang, J.-M. Facile assembly and electrochemical properties of α-Fe_2O_3@graphene aerogel composites as electrode materials for lithium ion batteries. *Mater. Chem. Phys.* **2016**, *182*, 190–199. [CrossRef]
15. Ji, L.W.; Lin, Z.; Alcoutlabi, M.; Zhang, X.W. Recent developments in nanostructured anode materials for rechargeable lithium-ion batteries. *Energy Environ. Sci.* **2011**, *4*, 2682–2699. [CrossRef]
16. Guo, J.; Li, J.; Huang, Y.; Zeng, M.; Peng, R. Novel mesoporous TiO_2 spheres as anode material for high-performance lithium-ion batteries. *Mater. Lett.* **2016**, *181*, 289–291. [CrossRef]
17. Han, H.; Song, T.; Bae, J.-Y.; Nazar, L.F.; Kim, H.; Paik, U. Nitridated TiO_2 hollow nanofibers as an anode material for high power lithium ion batteries. *Energy Environ. Sci.* **2011**, *4*, 4532–4536. [CrossRef]
18. Ryu, M.-H.; Jung, K.-N.; Shin, K.-H.; Han, K.-S.; Yoon, S. High Performance N-Doped Mesoporous Carbon Decorated TiO_2 Nanofibers as Anode Materials for Lithium-Ion Batteries. *J. Phys. Chem. C* **2013**, *117*, 8092–8098. [CrossRef]
19. Li, D.; Shi, D.Q.; Liu, Z.W.; Liu, H.K.; Guo, Z.P. TiO_2 nanoparticles on nitrogen-doped graphene as anode material for lithium ion batteries. *J. Nanopart Res.* **2013**, *15*. [CrossRef]
20. Zhang, J.J.; Yu, A.S. Nanostructured transition metal oxides as advanced anodes for lithium-ion batteries. *Sci. Bull.* **2015**, *60*, 823–838. [CrossRef]
21. Gao, R.; Jiao, Z.; Wang, Y.; Xu, L.; Xia, S.; Zhang, H. Eco-friendly synthesis of rutile TiO_2 nanostructures with controlled morphology for efficient lithium-ion batteries. *Chem. Eng. J.* **2016**, *304*, 156–164. [CrossRef]
22. Zuniga, L.; Agubra, V.; Flores, D.; Campos, H.; Villareal, J.; Alcoutlabi, M. Multichannel hollow structure for improved electrochemical performance of TiO2/Carbon composite nanofibers as anodes for lithium ion batteries. *J. Alloys Compd.* **2016**, *686*, 733–743. [CrossRef]
23. Ji, L.W.; Toprakci, O.; Alcoutlabi, M.; Yao, Y.F.; Li, Y.; Zhang, S.; Guo, B.K.; Lin, Z.; Zhang, X.W. Alpha-Fe2O3 Nanoparticle-Loaded Carbon Nanofibers as Stable and High-Capacity Anodes for Rechargeable Lithium-Ion Batteries. *ACS Appl. Mater. Interfaces* **2012**, *4*, 2672–2679. [CrossRef] [PubMed]
24. Wang, S.T.; Yang, Y.; Dong, Y.H.; Zhang, Z.T.; Tang, Z.L. Recent progress in Ti-based nanocomposite anodes for lithium ion batteries. *J. Adv. Ceram.* **2019**, *8*, 1–18. [CrossRef]
25. Gao, L.; Hu, H.; Li, G.J.; Zhu, Q.C.; Yu, Y. Hierarchical 3D TiO2@Fe2O3 nanoframework arrays as high-performance anode materials. *Nanoscale* **2014**, *6*, 6463–6467. [CrossRef] [PubMed]
26. Li, S.; Wang, M.Y.; Luo, Y.; Huang, J.G. Bio-Inspired Hierarchical Nanofibrous Fe3O4-TiO2-Carbon Composite as a High-Performance Anode Material for Lithium-Ion Batteries. *ACS Appl. Mater. Interfaces* **2016**, *8*, 17343–17351. [CrossRef]

27. Dylla, A.G.; Henkelman, G.; Stevenson, K.J. Lithium Insertion in Nanostructured TiO2(B) Architectures. *Acc. Chem. Res.* **2013**, *46*, 1104–1112. [CrossRef]
28. Yang, Z.; Du, G.; Meng, Q.; Guo, Z.; Yu, X.; Chen, Z.; Guo, T.; Zeng, R. Synthesis of uniform TiO2@carbon composite nanofibers as anode for lithium ion batteries with enhanced electrochemical performance. *J. Mater. Chem.* **2012**, *22*, 5848–5854. [CrossRef]
29. Liu, Y.; Yang, Y.F. Recent Progress of TiO2-Based Anodes for Li Ion Batteries. *J. Nanomater.* **2016**, *2016*. [CrossRef]
30. Guo, S.; Liu, J.; Qiu, S.; Wang, Y.; Yan, X.; Wu, N.; Wang, S.; Guo, Z. Enhancing Electrochemical Performances of TiO2 Porous Microspheres through Hybridizing with FeTiO3 and Nanocarbon. *Electrochim. Acta* **2016**, *190*, 556–565. [CrossRef]
31. Schweidler, S.; de Biasi, L.; Schiele, A.; Hartmann, P.; Brezesinski, T.; Janek, J. Volume Changes of Graphite Anodes Revisited: A Combined Operando X-ray Diffraction and In Situ Pressure Analysis Study. *J. Phys. Chem. C* **2018**, *122*, 8829–8835. [CrossRef]
32. Keppeler, M.; Shen, N.; Nageswaran, S.; Srinivasan, M. Synthesis of alpha-Fe2O3/carbon nanocomposites as high capacity electrodes for next generation lithium ion batteries: A review. *J. Mater. Chem. A* **2016**, *4*, 18223–18239. [CrossRef]
33. Fu, Y.; Wei, Q.; Lu, B.; Wang, X.; Sun, S. Stem-like nano-heterostructural MWCNTs/α-Fe2O3@TiO2 composite with high lithium storage capability. *J. Alloys Compd.* **2016**, *684*, 419–427. [CrossRef]
34. Fu, Y.; Wei, Q.; Wang, X.; Shu, H.; Yang, X.; Sun, S. Porous hollow [small alpha]-Fe2O3@TiO2 core-shell nanospheres for superior lithium/sodium storage capability. *J. Mater. Chem. A* **2015**, *3*, 13807–13818. [CrossRef]
35. Lv, X.; Deng, J.; Sun, X. Cumulative effect of Fe2O3 on TiO2 nanotubes via atomic layer deposition with enhanced lithium ion storage performance. *Appl. Surf. Sci.* **2016**, *369*, 314–319. [CrossRef]
36. Wang, H.-G.; Li, Y.-H.; Liu, W.-Q.; Wan, Y.-C.; Li, Y.-W.; Duan, Q. One-step facile synthesis of TiO2/Fe2O3 fiber-in-tube hierarchical heterostructures with improved lithium-ion battery performance. *RSC Adv.* **2014**, *4*, 23125–23130. [CrossRef]
37. Lian, X.; Cai, M.; Qin, L.; Cao, Y.; Wu, Q.-H. Synthesis of hierarchical nanospheres Fe2O3/graphene composite and its application in lithium-ion battery as a high-performance anode material. *Ionics* **2016**, *22*, 2015–2020. [CrossRef]
38. Meng, X.; Xu, Y.; Sun, X.; Xiong, L.; Wang, Q. Nitrogen-doped graphene assists Fe2O3 in enhancing electrochemical performance. *J. Power Sour.* **2016**, *326*, 389–396. [CrossRef]
39. Balogun, M.-S.; Wu, Z.; Luo, Y.; Qiu, W.; Fan, X.; Long, B.; Huang, M.; Liu, P.; Tong, Y. High power density nitridated hematite (α-Fe2O3) nanorods as anode for high-performance flexible lithium ion batteries. *J. Power Sour.* **2016**, *308*, 7–17. [CrossRef]
40. Zhang, X.; Chen, H.; Xie, Y.; Guo, J. Ultralong life lithium-ion battery anode with superior high-rate capability and excellent cyclic stability from mesoporous Fe2O3@TiO2 core-shell nanorods. *J. Mater. Chem. A* **2014**, *2*, 3912–3918. [CrossRef]
41. Wang, Z.Y.; Luan, D.Y.; Madhavi, S.; Hu, Y.; Lou, X.W. Assembling carbon-coated alpha-Fe2O3 hollow nanohorns on the CNT backbone for superior lithium storage capability. *Energy Environ. Sci.* **2012**, *5*, 5252–5256. [CrossRef]
42. Sides, C.R.; Li, N.C.; Patrissi, C.J.; Scrosati, B.; Martin, C.R. Nanoscale materials for lithium-ion batteries. *Mrs Bull.* **2002**, *27*, 604–607. [CrossRef]
43. Lee, S.; Ha, J.; Choi, J.; Song, T.; Lee, J.W.; Paik, U. 3D Cross-Linked Nanoweb Architecture of Binder-Free TiO2 Electrodes for Lithium Ion Batteries. *ACS Appl. Mater. Interfaces* **2013**, *5*, 11525–11529. [CrossRef]
44. Tammawat, P.; Meethong, N. Synthesis and Characterization of Stable and Binder-Free Electrodes of TiO2 Nanofibers for Li-Ion Batteries. *J. Nanomater.* **2013**, *2013*, 8. [CrossRef]
45. Agubra, V.A.; Zuniga, L.; Flores, D.; Campos, H.; Villarreal, J.; Alcoutlabi, M. A comparative study on the performance of binary SnO2/NiO/C and Sn/C composite nanofibers as alternative anode materials for lithium ion batteries. *Electrochim. Acta* **2017**, *224*, 608–621. [CrossRef]
46. Agubra, V.; Zuniga, L.; Flores, D.; Alcoutlabi, M. Forcespinning of Microfibers and their Applications in Lithium-ion and Sodium-ion Batteries. *ECS Trans.* **2016**, *72*, 57–65. [CrossRef]
47. Agubra, V.A.; De la Garza, D.; Gallegos, L.; Alcoutlabi, M. ForceSpinning of polyacrylonitrile for mass production of lithium-ion battery separators. *J. Appl. Polym. Sci.* **2016**, *133*. [CrossRef]

48. Agubra, V.A.; Zuniga, L.; De la Garza, D.; Gallegos, L.; Pokhrel, M.; Alcoutlabi, M. Forcespinning: A new method for the mass production of Sn/C composite nanofiber anodes for lithium ion batteries. *Solid State Ion.* **2016**, *286*, 72–82. [CrossRef]
49. Agubra, V.A.; Zuniga, L.; Flores, D.; Villareal, J.; Alcoutlabi, M. Composite Nanofibers as Advanced Materials for Li-ion, Li-O-2 and Li-S Batteries. *Electrochim. Acta* **2016**, *192*, 529–550. [CrossRef]
50. Flores, D.; Villarreal, J.; Lopez, J.; Alcoutlabi, M. Production of carbon fibers through Forcespinning (R) for use as anode materials in sodium ion batteries. *Mater. Sci. Eng. B* **2018**, *236*, 70–75. [CrossRef]
51. De la Garza, D.; De Santiago, F.; Materon, L.; Chipara, M.; Alcoutlabi, M. Fabrication and characterization of centrifugally spun poly(acrylic acid) nanofibers. *J. Appl. Polym. Sci.* **2019**, 136. [CrossRef]
52. Leng, X.; Wei, S.; Jiang, Z.; Lian, J.; Wang, G.; Jiang, Q. Carbon-Encapsulated Co3O4 Nanoparticles as Anode Materials with Super Lithium Storage Performance. *Sci. Rep.* **2015**, *5*, 16629. [CrossRef]
53. Wu, C.Y.; Li, X.P.; Li, W.S.; Li, B.; Wang, Y.Q.; Wang, Y.T.; Xu, M.Q.; Xing, L.D. Fe2O3 nanorods/carbon nanofibers composite: Preparation and performance as anode of high rate lithium ion battery. *J. Power Sour.* **2014**, *251*, 85–91. [CrossRef]
54. Qin, T.G.; Zeng, M.; Wu, X.; Wen, J.W.; Li, J. Fabrication of Fe2O3@TiO2 core-shell nanospheres as anode materials for lithium-ion batteries. *J. Mater. Sci.-Mater. Electron.* **2018**, *29*, 12944–12950. [CrossRef]
55. Zhong, Y.; Ma, Y.F.; Guo, Q.B.; Liu, J.Q.; Wang, Y.D.; Yang, M.; Xia, H. Controllable Synthesis of TiO2@Fe2O3 Core-Shell Nanotube Arrays with Double-Wall Coating as Superb Lithium-Ion Battery Anodes. *Sci. Rep.* **2017**, *7*, 40927.
56. Yang, Y.; Liu, Q.Y.; Cao, M.; Ju, Q.; Wang, H.Y.; Fu, R.Z.; Ji, H.M.; Yang, G. Enhanced electrochemical performance of alpha-Fe2O3 grains grafted onto TiO2-Carbon nanofibers via a Vapor-Solid reaction as anode materials for Li-Ion batteries. *Appl. Surf. Sci.* **2019**, *463*, 322–330. [CrossRef]
57. Peled, E.; Golodnitsky, D.; Ardel, G. Advanced model for solid electrolyte interphase electrodes in liquid and polymer electrolytes. *J. Electrochem. Soc.* **1997**, *144*, L208–L210. [CrossRef]
58. Jezowski, P.; Fic, K.; Crosnier, O.; Brousse, T.; Beguin, F. Lithium rhenium(VII) oxide as a novel material for graphite pre-lithiation in high performance lithiumion capacitors. *J. Mater. Chem. A* **2016**, *4*, 12609–12615. [CrossRef]
59. Agubra, V.A.; Fergus, J.W. The formation and stability of the solid electrolyte interface on the graphite anode. *J. Power Sour.* **2014**, *268*, 153–162. [CrossRef]